

Fine Grained Analysis and Optimization of Large Scale Automotive Radar Networks

Mohammad Taha Shah, *Graduate Student Member, IEEE*, Gourab Ghatak, *Member, IEEE*, and Shobha Sundar Ram, *Senior Member, IEEE*

Abstract—Advanced driver assistance systems (ADAS) enabled by automotive radars have significantly enhanced vehicle safety and driver experience. However, the extensive use of radars in dense road conditions introduces mutual interference, which degrades detection accuracy and reliability. Traditional interference models are limited to simple highway scenarios and cannot characterize the performance of automotive radars in dense urban environments. In our prior work, we employed stochastic geometry (SG) to develop two automotive radar network models: the Poisson line Cox process (PLCP) for dense city centers and smaller urban zones and the binomial line Cox process (BLCP) to encompass both urban cores and suburban areas. In this work, we introduce the meta-distribution (MD) framework upon these two models to distinguish the sources of variability in radar detection metrics. Additionally, we optimize the radar beamwidth and transmission probability to maximize the number of successful detections of a radar node in the network. Further, we employ a computationally efficient Chebyshev-Markov (CM) bound method for reconstructing MDs, achieving higher accuracy than the conventional Gil-Pelaez theorem. Using the framework, we analyze the specific impacts of beamwidth, detection range, and interference on radar detection performance and offer practical insights for developing adaptive radar systems tailored to diverse traffic and environmental conditions.

Index Terms—Stochastic geometry, Automotive radar, Poisson line Cox process, Binomial line Cox process, Meta distribution.

I. INTRODUCTION

Advanced driver assistance systems (ADAS) use automotive radars to improve safety through features such as adaptive cruise control, obstacle detection, and blind spot monitoring [1], [2]. The proliferation of these radars, however, introduces mutual interference between vehicles deteriorating the overall target detection accuracy [3], [4]. Traditionally, automotive radar interference has been studied using simple distributions of vehicles on highways using ray-tracing [5]. Similarly, recent works have employed stochastic geometry (SG) to model automotive radar networks on highways, analyzing detection performance in terms of mean signal-to-interference ratio (SIR) [6]. However, these models do not accurately emulate complex urban environments with diverse street geometries and vehicular conditions. Accurate spatial distribution models of automotive radar vehicles are essential for optimizing radar network performance and effectively mitigating mutual interference.

In our previous work, we considered two SG-based frameworks for modeling complex urban environments: the doubly stochastic homogeneous Poisson line Cox process (PLCP) and

the non-homogeneous binomial line Cox process (BLCP) [7]. Here, the line processes model the random distribution of streets within an area, while point processes model the random distribution of vehicles on a particular street. The PLCP has uniform street and vehicular densities, suitable for small local regions within a city, while the BLCP accounts for the heterogeneity of vehicular densities in areas with hierarchical street structures (e.g., highways, local streets, intersections), making it more appropriate for citywide scenarios. These models enable researchers to derive analytical expressions for the average detection probability of all the nodes in the network based on the SIR distribution [7].

For a deeper understanding, we must examine the detection performance of an individual radar rather than the average performance of all radars in the network. In particular, the simplistic SIR distribution combines all the random factors affecting a network, such as the density of interfering radars, channel fading conditions, etc., making it infeasible to isolate the impact of individual random elements on the overall radar detection performance. To address these limitations, the authors introduced the concept of meta distribution (MD) in [8], [9], which separates the different sources of randomness. A key challenge is the fact that closed-form expressions for the MD can only be derived for some simple scenarios, such as when considering signal power or SIR [10], using the Gil-Pelaez theorem [11]. However, for more complex models, it is generally infeasible to directly obtain analytic expressions. Thanks to the recent research presented in [12], several methods are now available for reconstructing MDs from the moments of conditional success probability (CSP).

Related Works: Modeling and characterization of radar interference has a rich literature, e.g., see [5], [6], [13]–[15]. In [16], the authors demonstrated significant degradation in detection due to the interference, while authors in [13] discussed the impact of ghost targets and reduced sensitivity from frequency modulated continuous wave (FMCW) radars on radar performance. Schipper *et al* [5] analyzed radar interference using traffic flow patterns to model vehicle distribution along roadways. The authors in [17] defined the spectral density distribution of orthogonal noise waveforms using an optimized Kaiser function and phase retrieval technique to reduce mutual interference between automotive radars.

More recent efforts exploited SG techniques to characterize radar interference across varying radar distributions and propose mitigation strategies. For instance, [6], [18] utilized a Poisson point process (PPP) to model vehicular one-dimensional radar distribution on highways to evaluate mean SIR. Similarly, [14] employed the strongest interferer approximation method to analyze radar detection range and false alarm rates. In [19], radar detection probability is derived

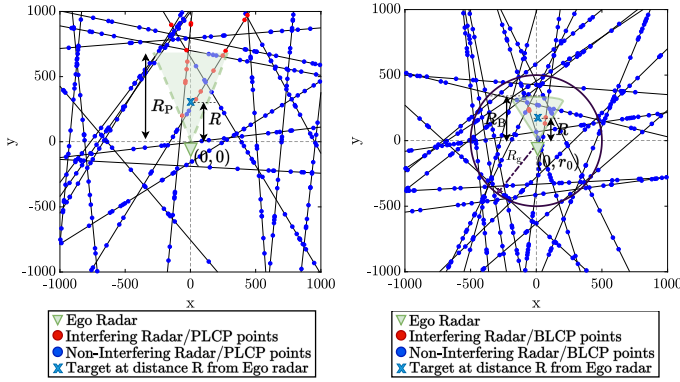


Fig. 1. (a) A realization of PLCP having $\lambda_L = 0.005 \text{ m}^{-2}$ and $\lambda = 0.005 \text{ m}^{-1}$, with ego radar present at origin, and (b) A realization of BLCP having $n_B = 50$ and $\lambda = 0.005 \text{ m}^{-1}$, with ego radar present at $(0, r_0)$.

for targets with fluctuating radar cross-sections (RCS) modeled with Swerling-I and Chi-square frameworks. Most of these analyses focus on two-lane traffic scenarios; however, multi-lane interference was addressed in [15] through a marked point process model. Using a PPP model, the study in [20] evaluated interference scenarios and proposed a centralized framework leveraging vehicle-to-everything (V2X) communication to allocate spectrum resources and minimize radar interference. Likewise, authors in [21] introduce a vehicular ad hoc networking (VANET)-assisted scheme that employs a time division multiple access (TDMA)-based medium access control (MAC) protocol to coordinate radar spectrum access among vehicles, enhancing interference mitigation. A distributed networking protocol for wireless radar control and interference mitigation was proposed in [22]. In [23], the authors introduced multiple spectrum-sharing strategies to mitigate interference in a vehicular radar network modeled as an Matern hardcore point process (MHCP) model in two-lane and multi-lane scenarios. In [24] authors proposed a TDMA scheme for coordinated interference mitigation, evaluated in terms of delay, interference-free radar capacity, interference probability, and control overhead.

The traditional metrics in SG are limited to providing an expected view of the system performance. In this regard, the MD framework has been widely utilized to study fine-grained aspects of wireless communication networks, [25]–[33] ranging from cellular networks, low earth orbit (LEO) satellite networks and UAV assisted networks. The authors in [34] proposed a trans-dimensional PPP (TPPP) model to analyze complex vehicular communication networks while accounting for street geometry and fading conditions. Authors in [35] investigated the SIR MD to understand the link performance in interference-limited wireless networks. They demonstrate that in Poisson networks, with independent fading and path loss, the SIR MD can be expressed as a product of the SIR threshold (β) and a function of reliability (t) within a specific region, i.e., (β, t) defined by the fading statistics. Despite its widespread use in analyzing cellular and ad-hoc networks, the application of MD in studying automotive radar performance is limited, especially in complex urban geometries.

A. Contributions, Organization, and Notation

In this study, we characterize two SG models tailored for distinct urban contexts for automotive radars: (i) PLCP model for densely populated city centers and smaller urban regions, and (ii) the BLCP model, which encompasses both central and suburban areas to offer a comprehensive view of the city. For each model, we derive analytical frameworks to evaluate the number of successful detections by an ego radar, the corresponding detection probability, and optimal system parameters to maximize the detection performance. The major contributions of this work are summarized as follows:

- We first derive the expected number of successful detections by an ego radar within both the PLCP and the BLCP frameworks. This is achieved by utilizing the average lengths of Poisson line process (PLP) and binomial line process (BLP) lines present within the bounded radar sector, providing a robust foundation for understanding radar performance. Subsequently, we propose an optimization framework to calculate the optimal beamwidth.
- We derive an analytical expression of the MD of signal fraction (SF) and SIR. Subsequently, we reconstruct the MD using moments leveraging techniques such as the Chebyshev-Markov (CM) bound method. This approach offers insights into the individual detection performance of vehicles, enhancing our understanding of radar effectiveness in real-world scenarios.
- Utilizing the first negative moment of SF MD, we derive metrics for the first successful detection, leveraging which we optimize transmission probability. This optimization benefits cognitive radars, enabling adaptive adjustments to transmission strategies based on real-time environmental conditions and interference levels.

In section II, we first introduce the network geometry and define the channel model along with the channel access scheme. In Section III, we derive the average number of potential targets that lie within the radar sector for both the PLCP and BLCP models. In section IV, we derive the MD of SF and define the MD reconstruction process. In section V, we plot all the numerical results highlighting the optimization strategies and the insights a network operator can draw from them. Finally, the paper concludes in section VI. To differentiate the notations between the two Cox process models, we use subscript of ‘ $k = P$ ’ for PLCP and ‘ $k = B$ ’ for BLCP models. For example, line processes are identified using calligraphic letters such as \mathcal{P} , thus \mathcal{P}_P denotes PLP and \mathcal{P}_B denotes BLP. Likewise, point processes are identified using the symbol Φ_P for PLCP, and Φ_B for BLCP. A BLP usually consists of n_B lines.

II. SYSTEM MODEL AND NETWORK GEOMETRY

Urban street networks show variability in street density and orientation, posing challenges in modeling, analyzing, and optimizing automotive radar system performance. In our previous work [7] we highlighted the non-homogeneity of real-world road networks Table II of [7] illustrates a stochastic distribution of streets characterized by both density and orientation. To address this, we model the street network

as a stochastic line process. Specifically, we use a PLP to represent local city regions with relatively homogeneous street distributions and a BLP to capture the variations in street density between urban centers and suburbs.

1) *PLCP*: In the PLP model, streets are represented as a set of random lines, $\mathcal{P}_P = \{L_1, L_2, \dots\}$, in the two-dimensional xy Euclidean plane. One instance of this distribution is shown in Fig. 1(a). Each line L_i is defined by its distance r_i from the origin and the angle θ_i between its normal and the x -axis. The parameters (θ_i, r_i) correspond to a point q_i in the domain space defined as $\mathcal{D}_P \equiv [0, \pi) \times (-\infty, \infty)$, creating a one-to-one correspondence between lines in \mathcal{P}_P and points in \mathcal{D}_P . The number of points in any subset, $S \subset \mathcal{D}_P$, follows a Poisson distribution with parameter $\lambda_L |S|$, where $|S|$ is the Lebesgue measure of S , and λ_L represents urban street density. Without loss of generality, we position the ego radar at the origin, represented by the green triangle in the figure, with its antenna beam also shown in green. From Slivnyak's theorem, conditioning on the location of a point in a PPP is the same as an addition of a point at the origin to the PPP in the \mathcal{D}_P [36]. This results in a PLP, $\mathcal{P}_{P_0} = \mathcal{P}_P \cup L_0$, where L_0 corresponds to $(\theta_0, r_0) = (0, 0)$ and denotes the street/line containing the typical ego radar located at the origin.

On each line L_i , we model vehicles as an independent 1D PPP, Φ_{L_i} , with intensity λ , representing vehicular density. These are represented by blue dots in the figure. This leads to the construction of PLCP, $\Phi_P = \bigcup_{L_i \in \mathcal{P}_P} \Phi_{L_i}$ which is a doubly stochastic Poisson process. Following the Palm distribution of the PLCP, the point process is given by $\Phi_{P_0} = \Phi_P \cup \Phi_{L_0}$, where the line L_0 accounts for the traffic moving in the opposite direction (towards the ego vehicle) on the street where the ego vehicle is situated. Interference occurs when the ego radar and another vehicle's radar are within each other's beam sectors (to be defined soon). The interfering radars are indicated by red dots in the figure.

2) *BLCP*: The BLP model considers the network of streets as a finite set of lines, $\mathcal{P}_B = \{L_1, L_2, \dots, L_{n_B}\}$, in the 2D Euclidean plane. One such instance is shown in Fig. 1(b). Each line L_i corresponds to a point, $(\theta_i, r_i) \in \mathcal{D}_B \equiv [0, \pi) \times [-R_g, R_g]$, where \mathcal{D}_B is the domain space of BLP. Note that, unlike the PLP case, the generating points are restricted to a disk of radius R_g centered at the origin. The vehicle positions along each line L_i are modeled as independent 1D PPPs, Φ_{L_i} , with intensity λ . The complete distribution forms BLCP defined as $\Phi_B = \bigcup_{i=1}^{n_B} \Phi_{L_i}$. The overall process, accounting for vehicles in the opposite direction of the ego vehicle's street, is represented as $\Phi_{B_0} = \Phi_B \cup L_0$. Unlike the homogeneous PLCP, the inhomogeneous BLCP cannot be characterized from a single typical point but depends on the distance from the origin. Thus, without loss of generality, we consider the ego radar to be located at $(0, r_0)$, where r_0 is its distance from the origin. The maximum unambiguous range of the radar is R_B (to be defined soon). As in the PLCP scenario, interference occurs if the ego and interfering radars are within each other's maximum unambiguous range and beam width.

Figures. 1(a) and (b) highlight the stark contrast between the spatial structures of the PLCP and BLCP. In a PLCP-modeled network, the ego radar experiences uniform inter-

ference characteristics regardless of its location. However, in a BLCP-modeled network, the interference characteristics vary depending on the ego radar's position in the Euclidean plane. Specifically, in the BLCP, an ego radar located near the city center (i.e., within the generating circle) will encounter different statistical features, such as street and intersection density, compared to those observed outside the city center.

A. Interfering Set

We assume that the radars are mounted on the front and rear of a vehicle and Ω is the half-power beamwidth. The orientation of vehicles on L_i depends on the generating angle, θ_i , and the direction of the vehicular movement. Thus, the boresight direction of any radar on L_i is given by the two unit vectors: \mathbf{a} and $-\mathbf{a}$, where $\mathbf{a} = (-\sin \theta_i, \cos \theta_i)^T$. Assume that any radar is located at (x, y) such that $(x, y) \in \Phi_{k_0}$. Any interfering radar represented as a point in the Euclidean plane $(p, q) \in \Phi_{k_0}$, lies in the antenna's beam sector of radar located at (x, y) if the angle made by the displacement vector between $(p, q) - (x, y)$ and the boresight direction exceeds $\cos \Omega$. Therefore, the radar sector is uniquely characterized by $\mathcal{R}_{(x,y),k}^+$ and $\mathcal{R}_{(x,y),k}^-$ as a function of (x, y) and Ω . Based on this, we define the *closed* interior region of the radar sector for any Cox point as

Definition 1. *The radar sector of a radar located at $(x, y) \in \Phi_{k_0}$ such that $x \cos \theta_i + y \sin \theta_i = r_i$ and $(\theta_i, r_i) \in \mathcal{D}_k$ for boresight direction \mathbf{a} is*

$$\mathcal{R}_{(x,y),k}^+ = \left\{ (p, q) \in \mathbb{R}^2 : \frac{((p, q) - (x, y)) \cdot \mathbf{a}}{\|(p, q) - (x, y)\|} > \cos \Omega, \right. \\ \left. \|(p, q) - (x, y)\| \leq R_k \right\}.$$

In the case of PLCP, the radar sector of ego radar is characterized by $(\theta_i, r_i) = (0, 0)$, and $(x, y) = (0, 0)$ since the ego radar is situated at the origin with its street oriented towards the y -axis. For BLCP the ego radar has $(x, y) = (0, r_0)$. The radar sectors formed by the automotive radar is *bounded*. For both PLCP and BLCP analysis, we assume the radar has a maximum operational range R_k where $k = P$, or $k = B$, meaning it cannot detect targets beyond this range. In real-world conditions, radar detection is also limited by blockages like buildings. Thus R_k represents the line-of-sight (LOS) range, and any radar outside this range will not interfere with the ego radar's detection performance. The ego radar at any position only experiences interference from the Cox points that lie within its radar sector, and the ego radar is in their radar sector. If the ego radar has \mathbf{a} as the boresight direction, then only the radars with boresight direction $-\mathbf{a}$ can contribute to interference. We generalize the set of interfering points as follows:

Definition 2. *For any Φ_{k_0} , the set of Cox points Φ_k^I that cause interference at the ego radar is*

$$\Phi_k^I = \bigcup_{(p,q) \in \Phi_{k_0}} \left\{ (p, q) : \right.$$

$$\left(\mathbf{1} \left((0, r) \in \mathcal{R}_{(p,q),k}^+ \right) + \mathbf{1} \left((0, r) \in \mathcal{R}_{(p,q),k}^- \right) \right) \cdot \left(\mathbf{1} \left((p, q) \in \mathcal{R}_{(0,r),k}^+ \right) + \mathbf{1} \left((p, q) \in \mathcal{R}_{(0,r),k}^- \right) \right) = 1 \left. \right\}.$$

where $\mathbf{1}(\cdot)$ is the indicator function, $\mathcal{R}_{(p,q),k}^+$ is closed interior region of any radar present at (p, q) , and $(0, r)$ is the location of ego radar, and $k \in \{P, B\}$. In the case of PLCP, the ego radar is at the origin, thus $r = 0$, and in BLCP, $r = r_0$.

The above definition outlines the set of interfering automotive radars Φ_k^I , having coordinates (p, q) that cause interference at the ego radar. If ego radar is within the radar sector of automotive radar present at (p, q) i.e., $\mathbf{1} \left((0, r) \in \mathcal{R}_{(p,q),P}^+ \right) + \mathbf{1} \left((0, r) \in \mathcal{R}_{(p,q),P}^- \right)$, and the automotive radar located at (p, q) is in the interior region of ego radar i.e., $\mathbf{1} \left((p, q) \in \mathcal{R}_{(0,r),P}^+ \right) + \mathbf{1} \left((p, q) \in \mathcal{R}_{(0,r),P}^- \right)$, only then radar at (p, q) will be an element of Φ_k^I .

B. Channel Access, SIR, and SF

In our previous work [7], we assumed that all the neighboring radars transmit continuously, which creates a very high probability of disturbance due to mutual interference. In civilian radar networks of high density, one consideration for tackling mutual interference is to enable vehicular radars to cognitively turn on transmissions based on ambient channel conditions. In this work, we study this concept by considering a simple ALOHA access protocol [37]. All the vehicles, including the ego radar, attempt to detect a target with probability p in this scheme. We refer to p as the transmission probability, as the vehicle needs to transmit the radar signal to be able to perform detection. Thus, each interference term is weighted using an indicator function $\mathbf{1}(\cdot)$ to denote whether the vehicle is transmitting or not. Let the set of locations of the interfering nodes be denoted by $\mathcal{C} \subset \Phi_k^I$. The ego radar receives the reflected signal power from the target vehicle with strength $S = \gamma \sigma_c P R^{-2\alpha}$, where, $\gamma = \frac{G_t}{(4\pi)^2} A_e$, A_e is the effective area of the receiving antenna aperture, G_t is the gain of the transmitting antenna, P is the transmit power, α is the path-loss exponent, and σ_c is fluctuating radar cross-section of target at distance R . The interference at the ego radar from either PLCP or BLCP caused by a single interfering radar situated at a distance w_k from the ego radar is expressed as $\mathbf{I}_k = P \gamma h_{\mathbf{w}_k} \|\mathbf{w}_k\|^{-\alpha}$, where $h_{\mathbf{w}_k}$ is the fading power. Accordingly, the SIR at the ego radar is

$$\xi_k = \frac{\gamma \sigma_c P R^{-2\alpha}}{\sum_{\mathbf{w}_k \in \Phi_k} 4\pi \gamma P h_{\mathbf{w}_k} \|\mathbf{w}_k\|^{-\alpha} \mathbf{1}(\mathbf{x} \in \mathcal{C})}. \quad (1)$$

In the MD analysis, we utilize SF rather than SIR as the main parameter. The justification for this choice is clarified in Section IV. SF is defined as the ratio of signal power to total received power. i.e., $\text{SF} = \frac{S}{S + \mathbf{I}_P}$, or $\text{SF} = \frac{\text{SIR}}{\text{SIR} + 1}$. In this scheme, the SF is defined as,

$$\text{SF}_k = \frac{\gamma \sigma_c P R^{-2\alpha}}{\gamma \sigma_c P R^{-2\alpha} + \sum_{\mathbf{w}_k \in \Phi_k} 4\pi \gamma P h_{\mathbf{w}_k} \|\mathbf{w}_k\|^{-\alpha} \mathbf{1}(\mathbf{x} \in \mathcal{C})}, \quad (2)$$

where \mathcal{C} is the set of locations of active interfering vehicles.

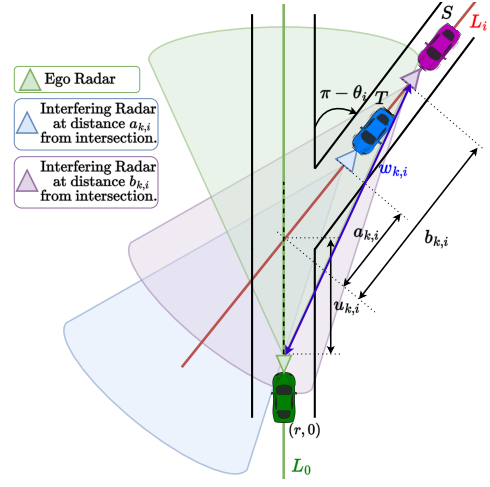


Fig. 2. Illustration of a scenario where two radars are present at the edge point of the line L_i inducing interference.

C. Interfering Distance

We observed from Fig 1. (a) and (b) that all the automotive radars emulated as Cox points do not cause interference (indicated by blue dots). Instead, interference is caused at the ego radar only when both the ego radar and the interfering radar are simultaneously within each other's radar sectors (indicated by red dots). The impact of the interfering radars located on the ego radar's street and the remaining streets on the detection performance of the ego radar is determined by the interfering distance $v_{B,i}$, the section of L_i wherein if a radar is present, it will contribute to the interference experienced by the ego radar. In order to derive $v_{B,i}$, we note that the distance from the ego radar to the intersection of the L_i^{th} line is $d_i = u_i - r_0 = \frac{r_i}{\sin \theta_i} - r_0$, where the angle of intersection is equal to the generating angle θ_i of the intersecting line. The distance between the interfering radar on L_i from the intersection point is $v_{k,i}$, referred to as the interfering distance. Figure 2 illustrates an ego radar with a green radar sector on L_1 and radars mounted on other vehicles, S and T , on L_i , with red and purple beams. Specifically, S and T are at a distance $v_{k,i} = b_{k,i}$ and $v_{k,i} = a_{k,i}$ from the intersection point, respectively. These two distances ($a_{k,i}$ and $b_{k,i}$) represent the bounds of $v_{k,i}$ within which another radar will interfere with the ego radar. From Fig. 2, any other vehicle present behind the vehicle S will not cause interference. Likewise, any vehicle present after vehicle T also will not cause interference. This is because the vehicles present behind S and after T will not mutually interfere with ego radar. The values of $a_{k,i}$ and $b_{k,i}$ for the different scenarios are presented in Lemma 1 and Theorem 1 of [7] for PLCP and BLCP respectively. Correspondingly, the distance from the ego radar to the interfering radar is then given as

$$w_{k,i} = \begin{cases} v_{k,i} & i = 0 \\ \sqrt{(d_i + v_{k,i} |\cos \theta_i|)^2 + (v_{k,i} \sin \theta_i)^2} & \text{otherwise.} \end{cases}$$

III. AVERAGE NUMBER OF POTENTIAL TARGETS

In this section, we determine the average number of potential targets that are located within the radar

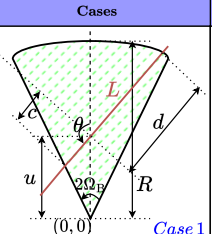
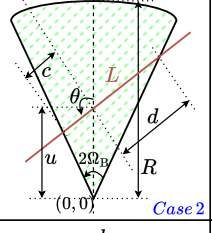
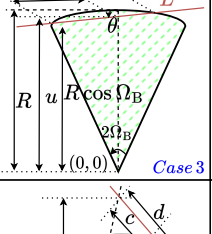
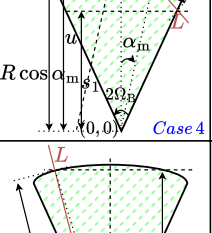
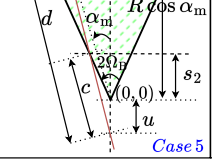
Cases	Length of PLP lines for different five cases
 <p>Case 1</p>	$c = \frac{u \tan \Omega}{\sin \theta + \cos \theta \tan \Omega}$ $d = \sqrt{R^2 - u^2 \sin^2 \theta} - u \cos \theta$ $p_1 = c + d$
 <p>Case 2</p>	$c = \frac{u \tan \Omega}{\sin \theta + \cos \theta \tan \Omega}$ $d = \frac{u \tan \Omega}{\sin \theta - \cos \theta \tan \Omega}$ $p_2 = c + d$
 <p>Case 3</p>	$c = \sqrt{R^2 - u^2 \sin^2 \theta} + u \cos \theta$ $d = \sqrt{R^2 - u^2 \sin^2 \theta} - u \cos \theta$ $p_3 = c + d$
 <p>Case 4</p>	$c \cos \theta = u - R \cos \alpha_m$ $d \cos \theta = u - s_1$ $s_1 = \frac{u \tan \theta }{ \tan \theta + \tan \Omega}$ $p_4 = d - c$
 <p>Case 5</p>	$c \cos \theta = u + s_2$ $d \cos \theta = u + R \cos \alpha_m$ $s_2 = \frac{u \tan \theta }{ \tan \theta - \tan \Omega}$ $p_5 = d - c$

Fig. 3. The figure illustrates different cases of a BLP line intersecting line L_0 . Case 1 to 5 correspond to 5 different cases to find l , i.e., from $l = p_1$ to $l = p_5$.

antenna's main lobe. This involves characterizing the average number of Cox points $n_k(R)$ in the beam sector of the ego radar with the distance to target as R . We identify $\mathcal{N}_{(0,r)}^+(R)$ as a collection of points (p, q) , lying within the target range of ego radar, $\mathcal{N}_{(0,r)}^+(R) = \left\{ (p, q) \in \mathbb{R}^2: \frac{q}{\sqrt{p^2 + (q-r)^2}} > \cos \Omega, \sqrt{p^2 + (q-r)^2} \leq R \right\}$, where $r = 0$ in case of PLCP and $r = r_0$ in case of BLCP. Next, we note that $n_k(R)$ depends on the average length of PLP or BLP lines inside $\mathcal{N}_{(0,r)}^+(R)$.

Definition 3. The average number of Cox points inside $\mathcal{N}_{(0,r)}^+(R)$ is

$$n_k(R) = \lambda l_k(R) = \lambda \mathbb{E}_{\mathcal{P}_{k_0}} \left[\left| L \cap \mathcal{N}_{(0,r)}^+(R) \right|_1 \right], \quad (3)$$

where $|\cdot|_1$ is the Lebesgue measure in one dimension and L

is a line of the PLP or BLP.

A. Average number of PLCP points in $\mathcal{N}_{(0,0)}^+(R)$

First, we determine the average length of a single line within $\mathcal{N}_{(0,0)}^+(R)$, in the following Lemma 1.

Lemma 1. The length of a line parameterized by (θ, r) present inside the radar sector $\mathcal{N}_{(0,0)}^+(R)$ of half beamwidth Ω and distance to target R is,

$$l = \begin{cases} p_0 = R_P; & \text{for } (\theta, r) = (0, 0) \\ p_1 = \frac{u \tan \Omega}{|\sin \theta| + |\cos \theta| \tan \Omega} + \sqrt{R^2 - u^2 \sin^2 \theta} - u |\cos \theta|; & \text{for } 0 \leq u \leq R, \text{ and } \theta \in \{[0, \alpha_n] \cup [\pi - \alpha_n, \pi]\} \\ p_2 = \frac{2u \sin \theta \tan \Omega}{\sin^2 \theta - \cos^2 \theta \tan^2 \Omega}; & \text{for } 0 \leq u \leq R \cos \Omega, \\ & \text{and } \theta \in [\alpha_n, \pi - \alpha_n] \\ p_3 = 2\sqrt{R^2 - u^2 \sin^2 \theta}; & \text{for } R \cos \Omega \leq u \leq R \\ & \text{and } \theta \in [\alpha_n, \pi - \alpha_n] \\ p_4 = \left(R \cos \alpha_m - \frac{u |\tan \theta|}{|\tan \theta| + \tan \Omega} \right) |\sec \theta|; & \\ \text{for } R < u \leq R(\cos \Omega + |\cot \theta| \sin \Omega), \text{ and } \theta \in [0, \pi] \\ p_5 = \left(R \cos \alpha_m - \frac{u |\tan \theta|}{|\tan \theta| - \tan \Omega} \right) |\sec \theta|; & \\ \text{for } R(\cos \Omega - |\cot \theta| \sin \Omega) \leq u < 0, \text{ and } \theta \in (\pi, 2\pi] \\ 0; & \text{otherwise} \end{cases} \quad (4)$$

where $\alpha_n = \arctan \left(\frac{R \sin \Omega}{R \cos \Omega - u} \right)$, and $\cos \alpha_m = \frac{u}{R} \sin^2 \theta + \sqrt{\frac{u^2}{R^2} (\sin^4 \theta - \sin^2 \theta) + \cos^2 \theta}$.

Proof. In order to determine the length of a line L within the radar sector, we have to carefully consider different cases of generating angle θ and the intersecting distance u . Depending on point of intersection and θ there are 6 different cases to find l corresponding to p_j where $j = \{0, 1, \dots, 5\}$. The value of $l = p_0$ is due to L_0 . Let us define four events based on the value of θ_i , which are as $A_1 = \{\theta: 0 \leq \theta \leq \frac{\pi}{2}\}$, $A_2 = \{\theta: \frac{\pi}{2} \leq \theta \leq \pi\}$, $A_3 = \{\theta: \pi \leq \theta \leq \frac{3\pi}{2}\}$, and $A_4 = \{\theta: \frac{3\pi}{2} \leq \theta \leq 2\pi\}$, corresponding to the generating present in four quadrants. As ego radar is located at the origin, the intersection occurs ahead of the ego radar if $0 \leq \theta \leq \pi$, which corresponds to cases 1-4, and the intersection occurs ahead of the ego radar if $\pi \leq \theta \leq 2\pi$ which corresponds to case 5. For case 1, L intersects one of the edge lines and circular curvature of the radar sector, while as in case 2, L intersects only the edge lines of the radar sector. In case 3 line L intersects only the arc of the sector. Case 4 and 5 are the same as case 1, except that in case 4, L intersects the y-axis outside the radar sector and ahead of the ego radar, whereas, in case 5, L intersects the y-axis behind the ego radar as shown in Fig. 3. In this proof, we will focus only on case 1, as the remaining cases have similar procedures to derive them. Consider for event A_1 , the value p_1 can be found as $p_1 = c + d$, where $c = \frac{u \tan \Omega}{\sin \theta + \cos \theta \tan \Omega}$ and $d = \sqrt{R^2 - u^2 \sin^2 \theta} - u \cos \theta$ follows from simple trigonometric operations. To determine p_1 for event A_2 as shown in Fig. 3, we take the modulus of

sine and cosine to accommodate the first two quadrants. Like wise for case 2 and 3, $p_j = c + d$, while as for case 4 and 5, $p_j = d - c$. By looking at Fig. 3, we can deduce that the remaining cases would follow a similar method of finding c and d while considering event A_1 and A_2 for cases 1-4, and event A_3 and A_4 for case 5. \square

Following Lemma 1, we derive the average length of PLP lines inside $\mathcal{N}_{(0,0)}^+(R)$ in Theorem 1.

Theorem 1. *In a PLP, the average length of line segments present inside the bounded radar sector $\mathcal{N}_{(0,0)}^+(R)$ is*

$$l_P(R) = \mathbb{E}_{\mathcal{P}_{P_0}} \left[\left| L \cap \mathcal{N}_{(0,0)}^+(R) \right|_1 \right] = 2\pi\lambda_L R \bar{l} + l_0, \quad (6)$$

where

$$\begin{aligned} \bar{l} = \frac{1}{2\pi R} & \left[\int_0^R \int_0^{\alpha_n} p_1 d\theta dr + \int_0^{R \cos \Omega} \int_{\alpha_n}^{\pi - \alpha_n} p_2 d\theta dr \right. \\ & + \int_{R \cos \Omega}^R \int_{\alpha_n}^{\pi - \alpha_n} p_3 d\theta dr + \int_R^{R(\cos \Omega + |\cot \theta| \sin \Omega)} \int_0^\pi \\ & \left. p_4 d\theta dr + \int_{R(\cos \Omega - |\cot \theta| \sin \Omega)}^0 \int_\pi^{2\pi} p_5 d\theta dr \right]. \end{aligned}$$

Remark 1. *Utilizing the result of Theorem 1 in definition 3, we observe that there is a linear relation between the average number of points in a radar sector and the intensity of the PLP. The same linear relation can be seen with the intensity of vehicles on the road. Therefore the average number of targets increase linearly with λ_L and λ .*

B. Average number of BLCP points in $\mathcal{N}_{(0,r_0)}^+(R)$

The average number of vehicles inside the ego radar's beam sector depends on the location of the radar due to the non-homogeneous nature of BLCP. In order to derive $n_B(R)$, first we derive the average length of BLP lines in $\mathcal{N}_{(0,r_0)}^+(R)$. Unlike the PLP, where the analysis follows a simpler approach of first determining the length of a single line inside the radar sector and then averaging the Poisson-distributed number of lines, the BLP utilizes the result of Theorem 2 from [38] where the line length density of BLP is derived as a function of distance from the origin. The theorem states that:

Lemma 2. *For a BLP having n_B lines within a disk of radius R_g , the line length density at a distance r from origin is,*

$$\rho(r) = \begin{cases} \frac{n_B}{2R_g}, & \text{if } r \leq R_g \\ \frac{n_B}{\pi R_g} \arcsin\left(\frac{R_g}{r}\right) & \text{if } r > R_g. \end{cases} \quad (7)$$

The above lemma shows that $\rho(r)$ first remains constant up to R_g , and then decreases as $\mathcal{O}(r)$, as $r \rightarrow \infty$. In other words, the street networks become less dense as we move towards the suburbs. We integrate the line length density for a bounded radar sector based on the location of ego radar, which gives us the average length of BLP lines inside $\mathcal{N}_{(0,r_0)}^+(R)$,

Theorem 2. *In a BLP having n_B lines and generated within a disk of radius R_g , the average length of line segments inside $\mathcal{N}_{(0,r_0)}^+(R)$ is given by $l_B(R)$ in (5), where*

$$y_A = \frac{\sqrt{4R_g^2 r_0^2 - (R_g^2 + r_0^2 - R^2)^2}}{2r_0}, \quad m = \cot \Omega$$

$$l_B(R) = \begin{cases} \frac{n_B}{2R_g} \Omega R^2; \text{ for } r_0 \in [-R_g, R_g - R] \\ \frac{n_B}{2R_g} \left[R^2 \arcsin\left(\frac{y_B}{R}\right) + y_B \sqrt{R^2 - y_B^2} + R^2 \arcsin\left(\frac{y_A}{R}\right) + y_A \sqrt{R^2 - y_A^2} + R_g^2 \arcsin\left(\frac{y_A}{R_g}\right) + \right. \\ \left. y_A \sqrt{R_g^2 - y_A^2} - 2r_0 y_A - m y_A^2 \right] + \frac{2n_B}{\pi R_g} \int_0^{y_A} \int_{\sqrt{R_g^2 - x^2} + r_0}^{\sqrt{R_g^2 - x^2}} \arcsin\left(\frac{R_g}{\sqrt{x^2 + y^2}}\right) dy dx; \\ \text{ for } r_0 \in \left(R_g - R, \sqrt{R_g^2 - (R \sin \Omega)^2} - R \cos \Omega \right) \\ \frac{n_B}{2R_g} \left(R_g^2 \arcsin\left(\frac{y_C}{R_g}\right) + y_C \sqrt{R_g^2 - y_C^2} - m y_C^2 - 2r_0 y_C \right) + \frac{2n_B}{\pi R_g} \left[\int_0^{y_C} \int_{\sqrt{R_g^2 - x^2} + r_0}^{\sqrt{R_g^2 - x^2}} \arcsin\left(\frac{R_g}{\sqrt{x^2 + y^2}}\right) dy dx + \right. \\ \left. \int_{y_C}^{y_B} \int_{m x + r_0}^{\sqrt{R_g^2 - x^2} + r_0} \arcsin\left(\frac{R_g}{\sqrt{x^2 + y^2}}\right) dy dx \right]; \text{ for } r_0 \in \left(\sqrt{R_g^2 - (R \sin \Omega)^2} - R \cos \Omega, R_g \right) \\ \frac{2n_B}{\pi R_g} \int_0^{y_B} \int_{m x + r_0}^{\sqrt{R_g^2 - x^2} + r_0} \arcsin\left(\frac{R_g}{\sqrt{x^2 + y^2}}\right) dy dx; \text{ for } r_0 \in \{ (R_g, \infty) \cup (-\infty, -(R_g + R)) \} \\ \frac{n_B}{2R_g} \left[R^2 \arcsin\left(\frac{y_B}{R}\right) + y_B \sqrt{R^2 - y_B^2} + R_g^2 \arcsin\left(\frac{y_C}{R_g}\right) + y_C \sqrt{R_g^2 - y_C^2} + 2r_0 y_C - m (y_B^2 - y_C^2) \right] - \\ \frac{2n_B}{\pi R_g} \int_0^{y_C} \int_{m x + r_0}^{\sqrt{R_g^2 - x^2}} \arcsin\left(\frac{R_g}{\sqrt{x^2 + y^2}}\right) dy dx; \text{ for } r_0 \in \left[-\sqrt{R_g^2 - (R \sin \Omega)^2} - R \cos \Omega, -R_g \right) \\ \frac{n_B}{2R_g} \left[R^2 \arcsin\left(\frac{y_A}{R}\right) + y_A \sqrt{R^2 - y_A^2} + R_g^2 \arcsin\left(\frac{y_A}{R_g}\right) + y_A \sqrt{R_g^2 - y_A^2} + 2r_0 y_A \right] - \\ \frac{2n_B}{\pi R_g} \left[\int_0^{-y_A} \int_{-\sqrt{R_g^2 - x^2}}^{m x + r_0} \arcsin\left(\frac{R_g}{\sqrt{x^2 + y^2}}\right) dy dx + \right. \\ \left. \int_{-y_A}^{y_B} \int_{-\sqrt{R_g^2 - x^2} + r_0}^{m x + r_0} \arcsin\left(\frac{R_g}{\sqrt{x^2 + y^2}}\right) dy dx \right]; \text{ for } r_0 \in \left[-(R_g + R), -\sqrt{R_g^2 - (R \sin \Omega)^2} - R \cos \Omega \right) \end{cases} \quad (5)$$

$$y_B = R \sin \Omega, \quad y_C = \frac{-mr_0 \pm \sqrt{R_g^2(1+m^2) - r_0^2}}{1+m^2}.$$

Proof. See Appendix A. \square

IV. META DISTRIBUTION ANALYSIS

Traditional studies on radar performance analysis involved the derivation of the probability of missed detection and the probability of false alarms. But in this article, we study an automotive radar network modeled using stochastic spatial processes and use the MD of the SIR and SF for fine-grained performance analysis. In [7], authors relied on a single, simplified distribution of the SIR. However, this approach failed to capture the nuances of individual detection performance due to factors like fading and locations of the interfering vehicles. The MD of the SIR offers a more granular perspective by explicitly accounting for these different sources of randomness. Despite these advantages, the computation of MD often requires focusing on the moments of the underlying conditional distribution. This section explores the application of the MD for both PLCP and BLCP based radar framework.

A. Meta Distribution of SF

Compared to the MD of SIR, the MD of SF offers a key advantage: SF is supported on the compact interval $[0, 1]$ compared to the SIR MD's range that extends to positive infinity. The bounded support of SIR MD ensures that all positive moments of the SF always exist, eliminating the need for truncation techniques when analyzing its distribution. Our approach enables a detailed analysis of an individual automotive radar's performance within the network, focusing on per-link metrics like detection probability, delay, and performance variance. From (2), the MD of SF is derived as,

$$F_{p_{\text{SF}},k}(t_{\text{SF}}) = \mathcal{P}_{M,k}(\beta_{\text{SF}}, t_{\text{SF}}) = \mathbb{P}(p_{\text{SF},k}(\beta_{\text{SF}}) \geq t_{\text{SF}}) \\ = \mathbb{P}(\mathbb{P}(\text{SF}_k > \beta_{\text{SF}} | \Phi_{k_0}) \geq t_{\text{SF}}) \quad (8)$$

where $\beta_{\text{SF}} \in [0, 1]$ is the SF threshold, and $t_{\text{SF}} \in [0, 1]$ is the complementary cumulative density function (CCDF) threshold or reliability threshold. The CCDF of the random variable, $\mathbb{P}(\text{SF}_k > \beta_{\text{SF}} | \Phi_{k_0})$, is the MD of the SF, given by

$$p_{\text{SF},k}(\beta_{\text{SF}}) = \mathbb{P}(\text{SF}_k > \beta_{\text{SF}} | \Phi_{k_0}) = \\ \mathbb{P}\left(\sigma_{\text{c}} \geq \frac{\beta_{\text{SF}} \sum_{\mathbf{w}_k \in \Phi_{k_0}} 4\pi h_{\mathbf{w}_k} \|\mathbf{w}_k\|^{-\alpha} \mathbf{1}(\mathbf{x} \in \mathcal{C})}{R^{-2\alpha}(1-\beta_{\text{SF}})} \mid \Phi_{k_0}\right) \\ \stackrel{(a)}{=} \mathbb{E}_{h_{\mathbf{w}_k}} \left[\exp\left(\frac{-\beta_{\text{SF}} \sum_{\mathbf{w}_k \in \Phi_{k_0}} 4\pi h_{\mathbf{w}_k} \|\mathbf{w}_k\|^{-\alpha} \mathbf{1}(\mathbf{x} \in \mathcal{C})}{\bar{\sigma} R^{-2\alpha}(1-\beta_{\text{SF}})}\right) \right] \\ = \prod_{\mathbf{w}_k \in \Phi_{k_0}} p \mathbb{E}_{h_{\mathbf{w}_k}} \left[\exp\left(\frac{-\beta_{\text{SF}} 4\pi \gamma P h_{\mathbf{w}_k} \|\mathbf{w}_k\|^{-\alpha}}{\gamma \bar{\sigma} P R^{-2\alpha}(1-\beta_{\text{SF}})}\right) \right] + (1-p) \\ \stackrel{(b)}{=} \prod_{\mathbf{w}_k \in \Phi_{k_0}} \frac{p}{1 + \beta'_{\text{SF}} \|\mathbf{w}_k\|^{-\alpha}} + (1-p), \quad (9)$$

where $\beta'_{\text{SF}} = \frac{4\pi\beta_{\text{SF}}}{\bar{\sigma} R^{-2\alpha}(1-\beta_{\text{SF}})}$. Step (a) follows from the exponential distribution of σ_{c} having mean $\bar{\sigma}$, and step (b) follows by taking the expectation over fading $h_{\mathbf{w}_k}$.

Calculating the distribution of $p_{\text{SF},k}(\beta_{\text{SF}})$ directly is not feasible. Instead, the moments of the problem are calculated and subsequently converted into the distribution [12]. Examining the instances of $p_{\text{SF},k}(\beta_{\text{SF}})$ offers a valuable understanding of the fluctuation and dispersion of effective detection of the target. For instance, it enables us to analyze the mean local delay, representing the expected number of transmissions required for successful detection. The following two lemma give the moments of $p_{\text{SF},\text{P}}(\beta_{\text{SF}})$ and $p_{\text{SF},\text{B}}(\beta_{\text{SF}})$.

Lemma 3. *PLCP: The b -th moment of $p_{\text{SF},\text{P}}(\beta_{\text{SF}})$ where $b \in \mathbb{C}$ is given as*

$$M_{b,\text{P}}(\beta_{\text{SF}}) = \exp\left(-\lambda \int_0^{R_{\text{P}}} 1 - \left(\frac{p}{1 + \beta'_{\text{SF}} v_{\text{P}}^{-\alpha}} + 1 - p\right)^b dv_{\text{P}}\right. \\ \left. - \lambda_{\text{L}} \int_{\mathbb{R}^+} \int_0^{2\pi} 1 - \exp\left(-\lambda \int_{a_{\text{P}}}^{b_{\text{P}}} 1 - \left(\frac{p}{1 + \beta'_{\text{SF}} \|\mathbf{w}_{\text{P}}\|^{-\alpha}} + 1 - p\right)^b dv_{\text{P}}\right) d\theta dr\right).$$

where $\|\mathbf{w}_{\text{P}}\|$ is distance to interfering radar. Also, a_{P} , and b_{P} can be found using Lemma 2 in [7].

Proof. From (9) we get,

$$M_{b,\text{P}}(\beta_{\text{SF}}) = \mathbb{E}_{\Phi_{\text{P}_0}} \left[\prod_{\mathbf{w}_{\text{P}} \in \Phi_{\text{P}_0}} \frac{p}{1 + \beta'_{\text{SF}} \|\mathbf{w}_{\text{P}}\|^{-\alpha}} + (1-p) \right] \\ \stackrel{(d)}{=} \exp\left(-\lambda \int_0^{R_{\text{P}}} 1 - \left(\frac{p}{1 + \beta'_{\text{SF}} v_{\text{P}}^{-\alpha}} + 1 - p\right)^b dv_{\text{P}}\right. \\ \left. - \lambda_{\text{L}} \int_{\mathbb{R}^+} \int_0^{2\pi} 1 - \exp\left(-\lambda \int_{a_{\text{P}}}^{b_{\text{P}}} 1 - \left(\frac{p}{1 + \beta'_{\text{SF}} \|\mathbf{w}_{\text{P}}\|^{-\alpha}} + 1 - p\right)^b dv_{\text{P}}\right) d\theta dr\right).$$

Step (d) follows by applying the Laplace functional of the reduced PLCP palm distribution (See Lemma 4.12 [39]). \square

Lemma 4. *BLCP: The b -th moment of $p_{\text{SF},\text{B}}(\beta_{\text{SF}})$ where $b \in \mathbb{C}$ is given as*

$$M_{b,\text{B}}(\beta_{\text{SF}}) = \exp\left(-\lambda \int_0^{R_{\text{B}}} 1 - \left(\frac{p}{1 + \beta'_{\text{SF}} v_{\text{B}}^{-\alpha}} + 1 - p\right)^b dv_{\text{B}}\right) \\ \left[\frac{1}{2\pi R_{\text{g}}} \int_0^{R_{\text{g}}} \int_0^{2\pi} \exp\left(-\lambda \int_{a_{\text{B}}}^{b_{\text{B}}} 1 - \left(\frac{p}{1 + \beta'_{\text{SF}} \|\mathbf{w}_{\text{B}}\|^{-\alpha}} + 1 - p\right)^b dv_{\text{B}}\right) d\theta dr \right]^{n_{\text{B}}-1}.$$

where $\|\mathbf{w}_{\text{B}}\|$ is distance to interfering radar. Also, a_{B} , and b_{B} can be found using Theorem 1 in [7].

Proof. From (9) we get,

$$M_{b,\text{B}}(\beta_{\text{SF}}) = \mathbb{E}_{\Phi_{\text{B}_0}} \left[\prod_{\mathbf{w}_{\text{B}} \in \Phi_{\text{B}_0}} \frac{p}{1 + \beta'_{\text{SF}} \|\mathbf{w}_{\text{B}}\|^{-\alpha}} + (1-p) \right]$$

$$\begin{aligned}
&= \exp \left(-\lambda \int_0^{R_B} 1 - \left(\frac{p}{1 + \beta'_{\text{SF}} v_B^{-\alpha}} + 1 - p \right)^b dv_B \right) \left(\frac{p}{1 + \beta'_{\text{SF}} \|\mathbf{w}_B\|^{-\alpha}} + 1 - p \right) dv_B \Big) d\theta dr \Big]^{n_B} \\
&\left[\frac{1}{2\pi R_g} \int_0^{R_g} \int_0^{2\pi} \exp \left(-\lambda \int_{a_B}^{b_B} 1 - \left(\frac{p}{1 + \beta'_{\text{SF}} \|\mathbf{w}_B\|^{-\alpha}} + 1 - p \right)^b dv_B \right) d\theta dr \right]^{n_B - 1}. \quad (11)
\end{aligned}$$

where $\beta' = \frac{4\pi\beta}{\sigma R^{-2\alpha}}$, and β is the SIR threshold.

Proof. The proof of the corollary is straightforward and follows by taking $b = 1$ in Lemma 3 and 4. \square

Remark 2. Lemma 3 and 4, provide the moments of MD of SF for the PLCP and BLCP frameworks respectively. Here, $b = 1$ represents the first moment, and $b = -1$ represents the first negative moments, both having their respective significance in characterizing the system performance. The first moment $M_{1,k} \left(\beta_{\text{SF}} = \frac{\beta}{1+\beta} \right)$ gives the detection probability that an attempted detection by the ego radar of the target located at a distance R is successful. Using the first moment, one can also determine the number of successful detections $n_{D,k}$ of vehicles for a fixed target distance R (more details in Section V-A). Likewise the first negative moment $M_{-1,k} \left(\beta_{\text{SF}} = \frac{\beta}{1+\beta} \right)$ gives the mean local delay $\mathcal{M}_k = \frac{1}{p} M_{-1,k} \left(\frac{\beta}{1+\beta} \right)$ and it represents the delay in detecting a target (more details in Section V-B).

In Section V, we will discuss the insights gained by studying these moments, but first, we derive the detection probability of ego radar for PLCP and BLCP modeled automotive radar networks using the MD.

B. Detection Success Probability

The detection success probability at a threshold β is defined as the CCDF of SIR, $p_{D,Kk}(\beta) = \mathbb{P}[\text{SIR} > \beta]$. This represents the probability that an attempted detection by the ego radar of the target located at a distance R is successful.

Corollary 1. For the network where the locations of the vehicles are modeled as PLCP, (Φ_{P_0}) or BLCP (Φ_{B_0}) and $\beta_{\text{SF}} = \frac{\beta}{1+\beta}$, the first moment, $M_{1,k}(\beta_{\text{SF}})$, is the detection success probability of an ego radar given by

$$\begin{aligned}
&\text{PLCP: } M_{1,P} \left(\frac{\beta}{1+\beta} \right) = p_{D,P}(\beta) = \\
&\exp \left(-\lambda \int_0^{R_P} 1 - \left(\frac{p}{1 + \beta' v_P^{-\alpha}} + 1 - p \right) dv_P \right. \\
&\quad \left. - \lambda_L \int_{\mathbb{R}^+} \int_0^{2\pi} 1 - \exp \left(-\lambda \int_{a_P}^{b_P} 1 - \left(\frac{p}{1 + \beta' \|\mathbf{w}_P\|^{-\alpha}} + 1 - p \right) dv_P \right) d\theta dr \right). \quad (10)
\end{aligned}$$

and

$$\begin{aligned}
&\text{BLCP: } M_{1,B} \left(\frac{\beta}{1+\beta} \right) = p_{D,B}(\beta) = \\
&\exp \left(-\lambda \int_R^{R_B} 1 - \left(\frac{p}{1 + \beta' v_B^{-\alpha}} + 1 - p \right) dv_B \right) \\
&\left[\frac{1}{2\pi R_g} \int_0^{R_g} \int_0^{2\pi} \exp \left(-\lambda \int_{a_B}^{b_B} 1 - \left(\frac{p}{1 + \beta' \|\mathbf{w}_B\|^{-\alpha}} + 1 - p \right) dv_B \right) d\theta dr \right]^{n_B - 1}.
\end{aligned}$$

C. Reconstruction of MD of $p_{\text{SF},k}(\beta_{\text{SF}})$ from $M_{b,k}(\beta_{\text{SF}})$

It is not feasible to compute the MDs for most network models. In certain simple cases, the MDs can be estimated by considering the closest interferer. Another way is by applying the Gil-Pelaez (GP) theorem [11] we compute the MD using only imaginary moments as shown $F_{p_{\text{SF}}}(z) = 0.5 + \frac{1}{\pi} \int_0^{\infty} \frac{\Im(e^{-ju \log(z)} M_{ju})}{u} du$. The analytical evaluation of the integral is intractable in the case of SF or SIR MD, and the numerical approximation computation of imaginary moments is computationally challenging. Instead, we use the Chebyshev-Markov (CM) method recently proposed by Wang *et.al* in [12]. Here, the authors reconstruct MD using a finite sequence of moments based on the Hausdorff moment problem (HMP). Hausdorff demonstrated that the existence of a distribution is contingent upon the infinite sequence of moments being completely monotonic. Furthermore, if the distribution does exist, it is unique. In practice, we have a finite sequence of moments, leading to a truncated HMP. Thus for the values of $M_b(\beta_{\text{SF}})$ for b -th moments, we determine $F_{p_{\text{SF}}}$ such that

$$\int_0^1 z^b dF_{p_{\text{SF}}}(z) = M_b(\beta_{\text{SF}}) \quad (12)$$

for $b = \{1, \dots, n\}$ and $n \in \mathbb{N}$. If \mathcal{F}_n is the set of all possible F which solve (12) then the infimum and supremum of F at the point of interest x_0 , is given as $\inf_{F_{p_{\text{SF}}} \in \mathcal{F}_n} F_{p_{\text{SF}}}(x_0)$, and $\sup_{F_{p_{\text{SF}}} \in \mathcal{F}_n} F_{p_{\text{SF}}}(x_0)$. The CM method consists of taking the average of infima and suprema to approximate the MD of $p_{\text{SF}}(\beta_{\text{SF}})$. If we take n moments, the reconstructed MD, is $F_{p_{\text{SF}}}(x, t_{\text{SF}}) = \left(\inf_{F_{p_{\text{SF}}} \in \mathcal{F}_n} F_{p_{\text{SF}}}(x, t_{\text{SF}}) + \sup_{F_{p_{\text{SF}}} \in \mathcal{F}_n} F_{p_{\text{SF}}}(x, t_{\text{SF}}) \right)$.

Building upon prior work by Markov, their approach tackles the problem of finding the infimum and supremum of a distribution function $F_{p_{\text{SF}}}$ within a specific range $[0, 1]$. The key idea is constructing a special discrete distribution $F_{p_{\text{SF}}}^*$ with two important properties: (1) Prescribed Moments: $F_{p_{\text{SF}}}^*$ is designed to match the given finite sequence of moments $M_b(\beta_{\text{SF}})$, and (2) Concentrated Mass: The maximum possible probability mass p_0 is concentrated at a specific point of interest x_0 within the range. This concentrated mass at x_0 essentially creates a *worst-case scenario* distribution in terms of the range of $F_{p_{\text{SF}}}(x_0)$. Mathematically, the infimum of $F_{p_{\text{SF}}}(x_0)$ across all allowable distributions \mathcal{F}_n is equal to $F_{p_{\text{SF}}}^*(x_0^{-1})$. Conversely, the supremum is equal to $F_{p_{\text{SF}}}^*(x_0)$. In our case, we already have the moments of $p_{\text{SF}}(\beta_{\text{SF}})$ given in Lemma 3 and 4. Further, by leveraging the concept of jumps in a discrete distribution, where the jump locations x_i represent possible values and the jump heights p_i represent

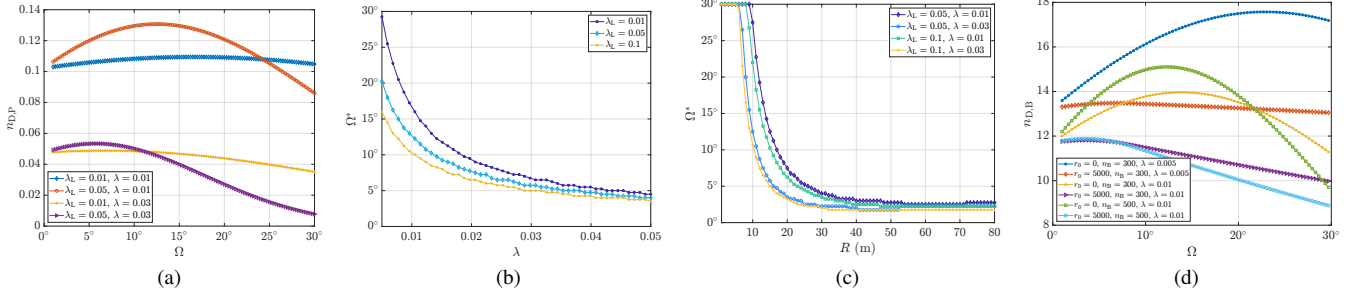


Fig. 4. (a) and (d) Number of successful detections versus Ω for PLCP and BLCP framework respectively, (b) and (c) Optimal beamwidth versus λ and R respectively for PLCP.

the corresponding probabilities. By carefully choosing these jumps and their heights, the constructed distribution F_{PSF}^* achieves the desired properties of matching moments and concentrating mass at the point of interest. The CM method provides a practical approach to approximate the MD by constructing a discrete distribution with prescribed moments. This approximation aligns with theoretical MD characteristics, allowing for efficient reconstruction of complex distributions while adhering to computational feasibility.

V. NUMERICAL RESULTS AND DISCUSSION

This section highlights the results from a typical automotive radar PLCP and BLCP framework. The radar parameters used for the numerical results are based on typical automotive radars obtained from [40]. Specifically, $P = 10$ dBm, $\bar{\sigma} = 30$ dBsm, $\alpha = 2$, $G_t = G_r = 10$ dBi, $f_c = 76.5$ GHz, $\beta = 1$ dB (SIR threshold), and $\beta_{SF} = 0.5$ (SF threshold). In all the plots, we assume $R = 15$ m, $\lambda = 0.01$ m⁻¹, $R_g = 1500$ m, $n_B = 300$, and $R_k = 500$ m unless specified otherwise.

A. Optimal Parameters

We denote the average number of successful detections, $n_{D,k}$, as the product of the probability of successful detection and the average number of potential targets present within the bounded radar beam of the ranging distance R , i.e., $n_{D,k} \geq n_k(R) \times p_{D,k} = \lambda_k p_{D,k}$. It is a measure for approximating the minimum number of successful detections, thus serving as a significant instrument for optimizing radar system design. Figure 4a shows the plot of $n_{D,P}$ with respect to beamwidth (Ω). From Remark 1, $n_P(R)$ has a linear relation with the intensity of the lines/streets and the intensity of vehicles on the road. Due to the symmetric structure of the radar sector and the homogeneous nature of PLCP, the same behavior of linearity follows with beamwidth, i.e., $n_P(R)$ increases linearly as Ω increases, while the detection probability decreases with increasing beamwidth [7]. As we take the product of $n_P(R)$ and $p_{D,P}$, $n_{D,P}$ first increases as $n_P(R)$ dominates $p_{D,P}$, then after a certain critical value of Ω , $p_{D,P}$ dominates $n_P(R)$, and $n_{D,P}$ then decreases. As the intensity of lines and the beamwidth increase, the average length of line segments within the radar sector also increases. However, the increase in λ_L and beamwidth results in a reduced probability of successful detection due to increased interference. Consequently, a trade-off exists between $p_{D,P}$

and the average length and an optimal beamwidth value, Ω^* , exists, for which $n_{D,P}$ is maximized and likewise for $n_{D,B}$, $\Omega^* = \arg \max n_{D,k}$. Fig.4d shows the plot of $n_{D,B}$ with respect to beamwidth and similar trade-off exists between $p_{D,B}$ and $n(R)$. Unlike PLCP, we find an optimal beamwidth, for which $n_{D,B}$ is maximized as a function of the location of ego radar.

In Fig. 4b we plot the optimal beamwidth Ω^* w.r.t λ for 3 different values of λ_L . The figure illustrates that the optimal beamwidth decreases with an increase in λ , eventually saturating. For a given value of λ , optimal beamwidth increases for increasing values of λ_L . Likewise, we find the optimal beamwidth as a function of distance to target R .

Figure. 4c illustrates the optimal beamwidth with respect to R for various values of λ_L and λ . We see that for smaller values of R , irrespective of the intensity of streets and radars, the optimal beamwidth remains constant at 30° . For the smaller value of $\lambda = 0.01$ m⁻¹, optimal beamwidth remains constant for a larger span of R as compared to the higher value of λ . Our analysis shows that the number of successful detections keeps increasing for smaller values of range R with the increasing beamwidth. This is because with very few interferers present and a small R , even if we increase beamwidth, the effect of the interferers is not sufficiently significant to limit $n_{D,P}$. Similarly when $\lambda_L = 0.05$ m⁻² and $\lambda = 0.01$ m⁻¹, the optimal beamwidth is constant at 30° for a larger range of R , as compared to $\lambda_L = 0.1$ m⁻² and $\lambda = 0.03$ m⁻¹. Eventually, optimal beamwidth plateaus to some value. Further, we see that for higher intensity values of interfering radars, the optimal beamwidth plateaus are quicker compared to lower values. When R is higher, the area of the radar sector is greater, including more interferers. Therefore, with the increase in R , the effect of interfering signal power received for higher λ_L and λ causes the optimal beam to saturate to lower values quicker as compared to the scenario when λ_L and λ are smaller.

Figures. 4(e) and (f) illustrate the optimal beamwidth as a function of r_0 , and R respectively for parameters $n_B = 300, 500$ and $\lambda = 0.005, 0.01$ m⁻¹. From a cognitive radar perspective, the optimum beamwidth for vehicles should be selected as the ego vehicle moves from one side of the city to the other side. Fig. 5a illustrates that the optimal beamwidth first increases then saturates as the vehicle moves into the city, and then decreases as the vehicle exits the city center. Due to fewer interferers at the outskirts, we would anticipate that the

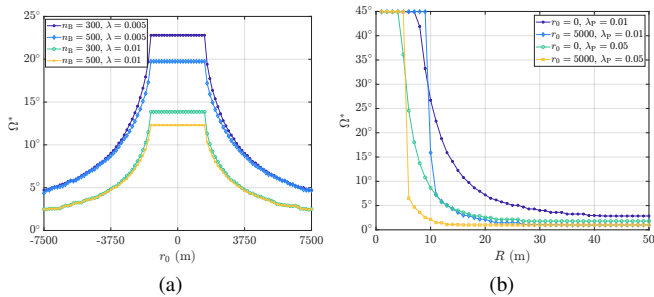


Fig. 5. (a) and (b) Optimal beamwidth versus r_0 and R respectively for BLCP.

ego radar can increase its beamwidth, here, to detect a larger number of targets. However, our analysis shows that we do not observe this in Fig. 5a. Instead, at the city's outskirts, having $\Omega > \Omega^*$ does not significantly increase the potential number of targets relative to the detection probability; thus, the optimal number of target detections occurs at smaller values of Ω . The main insight we obtain from this result is that *outside of the city center, the ego radar should prioritize monitoring vehicles traveling within its own lane rather than focusing excessively on those approaching from intersections*. For smaller values of $\lambda = 0.005 \text{ m}^{-1}$, the ego radar will encounter fewer interferers; thus, the optimal beamwidth has values larger as compared to $\lambda = 0.01 \text{ m}^{-1}$. We also see that at the outskirts of the city for a given λ , optimal beamwidth plateaus for $n_B = 300$ and 500 . This is because the impact of interference from the intersecting streets decreases, and only the interference from the ego radars street affects n_D .

Likewise, we find the optimal beamwidth w.r.t the distance to target R , as illustrated in Fig. 5b. When the ego radar operates outside the city center and at initial values of $R < 10$ m, the optimal beamwidth remains fixed at $\Omega = 45^\circ$, indicating that the ego radar can maintain the largest possible beamwidth. As R increases beyond 10 m with $\lambda = 0.01$, the ego radar should dynamically reduce its beamwidth from 45° to 15° . The optimal beamwidth in the case of $r_0 = 5000$ plateaus quickly while for $r_0 = 0$, the ego radar has to adjust the beamwidth by increasing the amount of R and plateauing slowly. As shown in Fig. 5b, the saturated beamwidth for a fixed λ is higher when $r_0 = 0$ than when $r_0 = 5000$, reflecting that at the outskirts, most potential targets are concentrated along L_0 , whereas at $r_0 = 0$, additional targets appear due to interfering lines. Consequently, at $r_0 = 5000$, the ego radar selects a narrower beamwidth at larger values of R to maintain a high detection probability.

B. Results on MD

1) *Reconstruction of MD*: In section IV, we noted that the MD are infeasible to solve, and we rely on the novel CM bound method. To determine the fitness of MD reconstructed through the CM bound method, we compute the Kolmogorov–Smirnov (K-S) distance which is the largest absolute difference between the CDFs of the two samples, offering a measurable indication of the similarity between the distributions, with values ranging between 0 and 1. The bounded nature of this metric provides an advantage over other

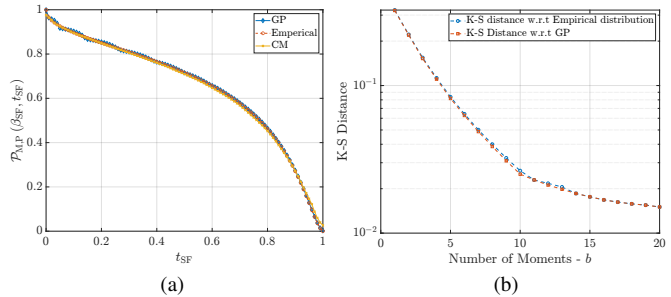


Fig. 6. (a) SF MD of an ego radar in PLCP framework generated through empirical, GP, and CM-bound methods, and (b) K-S distance between the CM-bound and empirical distribution, and the GP method, versus the number of moments

metrics, such as the Wasserstein distance and the Kullback-Leibler (KL) divergence, which can have a wide range of values and are not as easily interpretable. Compared to KL divergence, which measures the discrepancy between two probability distributions in terms of information loss, the KS distance has the benefit of being both symmetrical and non-parametric.

In Fig 6a, we plot the MD of SF in a PLCP framework for values of $\beta_{SF} = 10/(10 + 1)$, $\lambda_L = \lambda = 0.01$, and $\Omega = 15^\circ$, and benchmark the reconstructed MD using the CM bound method with the GP method, and the empirical distribution. From Fig. 6a, we see that for ten moments of $p_{SF}(\beta_{SF})$, the CM bound methods achieve a construction error of 0.01 with respect to the GP method and 0.005 with respect to the empirical distribution, demonstrating a high level of accuracy. As seen in Fig. 6a, the reconstructed MD through GP method and empirical distribution are approximately equal to each other, thus we can use any one of the methods to determine the fitness of MD generated through CM bound. Therefore, in Fig. 6b, we plot the K-S distance between the MD of CM bound w.r.t to both the GP and empirical methods. We take $b = \{1, \dots, 21\}$ and calculate moments using $M_b(\beta_{SF})$, and then employ these moments in reconstructing MD. The resulting K-S distance decreases as b increases, as shown in the plot. Any value of $b \geq 10$ offers a good match (i.e., the total distance is in $(0.005, 0.01]$). The only trade-off is that the computation time increases as we use more and more moments to reconstruct the MD. Thus, we conclude that the CM-bound method helps reconstruct MD with high accuracy. In all of the further results, we use the CM bound method to reconstruct the MD by taking 21 moments and using the reconstructed MD to derive results and insights.

2) Inference from reconstructed MD - $\mathcal{P}_{M,k}(\beta_{SF}, t_{SF})$:

We illustrate how the reconstruction of the MD can improve network efficiency and eventually mitigate the effect of interference. In the context of an MD reliability analysis (8), $\mathcal{P}_{M,k}(\beta_{SF}, t_{SF}) = y$ represents the probability that a fraction of $1 - y$ of users achieve a reliability level of t_{SF} at the threshold SF value of β_{SF} . By selecting the value of β_{SF} , we determine the reliability t_{SF} corresponding to a specific SF value β_{SF} , which represents the percentage of users who fail to achieve it. We identify the pairs (β_{SF}, t_{SF}) for $\mathcal{P}_{M,k}(\beta_{SF}, t_{SF}) = 0.1$ and 0.5 . This refers to the reliability

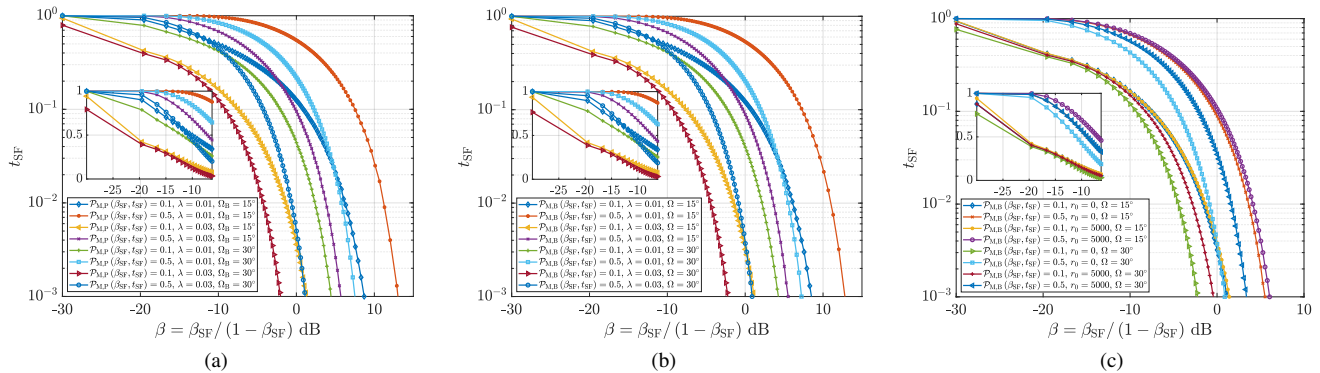


Fig. 7. Plot between t_{SF} and β_{SF} where $\mathcal{P}_{M,k}(\beta_{\text{SF}}, t_{\text{SF}}) = \{0.1, 0.5\}$ for the CM method at $n = 21$ for (a) PLCP framework, (b) BLCP framework with $r_0 = 0$, and (c) for BLCP framework for different values of r_0 .

of detecting a target and the SF threshold value at the 10th percentile and 50th percentile, indicating that 90% and 50% of users achieve or surpass this level of reliability, respectively. In our analysis, we assume $p = 1$, i.e., all radars are transmitting, and we vary β_{SF} from 0.001 to 0.99, which corresponds to β in the range of $[-29.99, 18.47]$ dB. We first discuss the MD results for PLCP, followed by BLCP.

PLCP: For PLCP, we see that from Fig. 7a, at $\beta = 0$ dB, $\lambda = 0.01$, and $\Omega = 15^\circ$, 90% of users can achieve detection probability with reliability level close to 0.125. In contrast, 50% of users can have reliability of $t_{\text{SF}} = 0.547$ in detecting a target. As the beam width increases from 15° to 30° , the reliability level for detecting a target decreases for all the users. Note that Fig. 4a only illustrates an average view of the network, i.e., the number of successful detections averaged across all automotive radars, while Fig. 7a offers insights about the deep network performance. For $\beta = -10$ dB and $\lambda = 0.03$, as Ω increases from 15° to 30° , the reliability decreases from $t_{\text{SF}} = 0.679$ to 0.447 in case $\mathcal{P}_{M,P}(\beta_{\text{SF}}, t_{\text{SF}}) = 0.5$, indicating that by increasing the beamwidth the reliability level for 50% of users decreases at a faster rate.

Another interesting insight that can be obtained from this analysis in Fig. 7a, is that 50% of users achieve the detection of a target with a reliability level of 0.97 at $\lambda = 0.01$, $\Omega = 15^\circ$, and $\beta = -10$ dB. When we increase the intensity of vehicles to 0.03, the reliability level falls to $t_{\text{SF}} = 0.679$; if we increase the beam width to 30° , the reliability, $t_{\text{SF}} = 0.84$. Thus, we get a higher reliability when the beamwidth of vehicles is increased as compared to if only the number of vehicles on streets increases. *Thus, if we want to have half of the vehicles perform reasonably well in detecting several targets, increasing the beamwidth is beneficial for smaller λ , while in dense urban areas with high vehicular density, we will have a better performance if we keep beamwidth small.*

BLCP: Next, we plot the MD results for the BLCP framework in Figs. 7(b) and (c). In Fig. 7b, we plot the t_{SF} w.r.t β for different values of $\mathcal{P}_{M,B}(\beta_{\text{SF}}, t_{\text{SF}})$, λ , and Ω when the ego radar is at the origin, i.e., $r_0 = 0$. Contrary to the PLCP, Fig. 7c shows how the reliability level changes as the location of the ego radar (r_0) varies across the city. For $\mathcal{P}_{M,B}(\beta_{\text{SF}}, t_{\text{SF}}) = 0.1, 0.5$, and $\Omega = 15^\circ$, the reliability threshold is same irrespective of r_0 . When the beamwidth is 15° , the interferers on the intersecting lines have a less

prominent effect than L_0 . Thus, the reliability threshold at different city locations is nearly constant as we have assumed a uniform λ across all lines. On the contrary, when $\Omega = 30^\circ$, at $\beta = -10$ dB, 90% of users in the city center achieve detection probability with a reliability level close to 0.119, while at the outskirts, i.e., $r_0 = 5000$ it is 0.148. For $r_0 = 5000$, and $\Omega = 30^\circ$, 90% of users have reliability level close to 0.4307 which increases to 0.5766 for 50% of users. Thus, the intensity of vehicles, λ , and Ω are two parameters that can be optimized so that per radar detection performance can be optimized.

3) *Optimization through MD:* In this section, we plot the metric which defines the delay in successfully detecting the target i.e., the mean local delay given as: $\mathcal{M}_k = \frac{1}{p} M_{-1,k} \left(\beta_{\text{SF}} = \frac{\beta}{1+\beta} \right)$. Consider a Bernoulli distribution; the first negative moment of this Bernoulli random variable represents the mean number of counts to get the first detection success. Therefore, if a radar transmits pulses with a probability p , then \mathcal{M}_k represents the pulse delay in detecting a target. From Fig. 8a, we observe that as the transmit probability increases, the local delay initially decreases because the transmitter tries to detect at a more frequent pace. However, a further increase in the transmit probability leads to a higher intensity of interfering automotive radar, which degrades detection probability and increases delay. This demonstrates that we can optimize the transmit probability to minimize the overall detection delay. Deriving this optimal probability is complex due to two opposing factors: increasing the transmit probability increases the frequency of detection attempts. However, this increases interference, reducing the detection success.

Figure. 8b shows the optimal transmit probability for minimizing the mean local delay in detecting a target w.r.t to the beamwidth of ego radar across various values λ_L and λ . As Ω increases, the optimal transmit probability p^* initially remains constant and then declines. The rate by which the optimal transmission probability decreases is higher for larger intensity values of streets and vehicles. For $\lambda_L = 0.01$ and $\lambda = 0.01, 0.03$, i.e., a sub-urban area, the optimal probability is greater than 0.5 for all the values of Ω , while as for the remaining values of λ_L and λ , optimal probability decreases as the beam width increases. Urban and dense urban areas show sensitivity to even slight variations of Ω .

Likewise for the BLCP framework, we plot the mean local

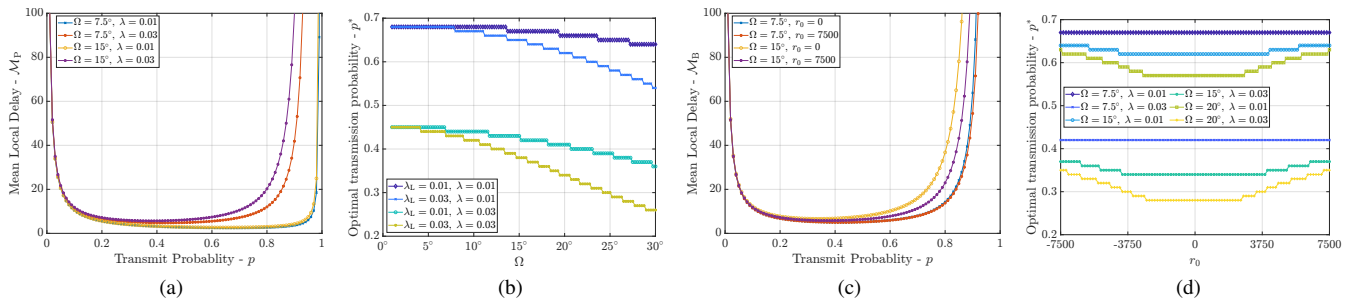


Fig. 8. Transmission probability versus the mean local delay of an ego radar for (a) PLCP, and (c) BLCP model, (b) optimal transmission probability versus beamwidth in PLCP model, and (d) optimal transmission probability versus r_0 for BLCP.

delay $\mathcal{M}_B = \frac{1}{p} M_{-1,B}(\beta_{SF})$ for an ego radar w.r.t p in Fig. 8c. We plot \mathcal{M}_B for two different values of $\Omega = 7.5^\circ, 15^\circ$, and $r_0 = 0, 7500$. We see that an optimal transmit probability exists for which the delay is minimized; we also observe that at the city center, the ego radar experiences a higher delay in successful target detection as compared to the outskirts of $r_0 = 7500$. Leveraging the data from Fig. 8c, we plot the optimal transmit probability p^* w.r.t location of ego radar in Fig. 8d. For network engineers, it is favorable to know the transmission probability for a cognitive automotive radar so as to maximize the overall network performance. Figure 8d, illustrates that for $\Omega = 7.5^\circ$, p^* remains constant at all values of r_0 irrespective of λ . For a small Ω , the ego radar experiences the same interference pattern across all locations as the interference contribution only comes due to interference present on line L_0 . While for $\Omega = 15^\circ, 20^\circ$ the p^* first decreases, then plateaus, and then again increases. The saturation region depends on the value of Ω and not λ . When ego radar operates outside the city, it may exhibit a higher p due to reduced interferences compared to its operation within the city center.

VI. CONCLUSION

We presented a comprehensive analysis of automotive radar performance under the frameworks of both PLCP and BLCP, yielding novel insights into optimizing automotive radar parameters. Notably, we derived the optimal beamwidth and transmission probability parameters w.r.t to the dynamic location of ego radar within and outside the city. These insights, achieved through our BLCP modeling approach, can enable cognitive radar systems to adapt and optimize detection capabilities in high-interference settings dynamically. We also demonstrated that the CM-bound method effectively reconstructs moment distributions with high accuracy, allowing for improved network efficiency and interference mitigation. By assuming a cognitively enabled vehicular radar network, we optimized the transmission frequency of the automotive radars so as to enhance target detection accuracy. This optimization allows for refined network efficiency and improved interference mitigation. These conclusions suggest practical frameworks for optimizing radar designs in urban and suburban areas with high traffic variability.

REFERENCES

- [1] I. Bilik *et al.*, “The rise of radar for autonomous vehicles: Signal processing solutions and future research directions,” *IEEE signal processing Magazine*, vol. 36, no. 5, pp. 20–31, 2019.
- [2] N. Lu *et al.*, “Connected vehicles: Solutions and challenges,” *IEEE internet of things journal*, vol. 1, no. 4, pp. 289–299, 2014.
- [3] M. Goppelt *et al.*, “Automotive radar—investigation of mutual interference mechanisms,” *Advances in Radio Science*, vol. 8, pp. 55–60, 2010.
- [4] S. Alland *et al.*, “Interference in automotive radar systems: Characteristics, mitigation techniques, and current and future research,” *IEEE Signal Processing Magazine*, vol. 36, no. 5, pp. 45–59, 2019.
- [5] T. Schipper *et al.*, “Simulative prediction of the interference potential between radars in common road scenarios,” *IEEE Transactions on Electromagnetic Compatibility*, vol. 57, no. 3, pp. 322–328, 2015.
- [6] A. Al-Hourani *et al.*, “Stochastic geometry methods for modeling automotive radar interference,” *IEEE Transactions on Intelligent Transportation Systems*, vol. 19, no. 2, pp. 333–344, 2017.
- [7] M. T. Shah *et al.*, “Modeling and Statistical Characterization of Large-Scale Automotive Radar Networks,” *arXiv:2408.13645*, 2024.
- [8] M. Haenggi, “Meta distributions—Part 1: Definition and examples,” *IEEE Communications Letters*, vol. 25, no. 7, pp. 2089–2093, 2021.
- [9] M. Haenggi, “Meta distributions—Part 2: Properties and interpretations,” *IEEE Communications Letters*, vol. 25, no. 7, pp. 2094–2098, 2021.
- [10] M. Haenggi, “The meta distribution of the SIR in Poisson bipolar and cellular networks,” *IEEE Transactions on Wireless Communications*, vol. 15, no. 4, pp. 2577–2589, 2015.
- [11] J. Gil-Pelaez, “Note on the inversion theorem,” *Biometrika*, vol. 38, no. 3-4, pp. 481–482, 1951.
- [12] X. Wang and M. Haenggi, “Fast Hausdorff Moment Transforms for Meta Distributions in Wireless Networks,” *IEEE Transactions on Wireless Communications*, 2023.
- [13] M. Goppelt *et al.*, “Analytical investigation of mutual interference between automotive FMCW radar sensors,” in *2011 German Microwave Conference*, pp. 1–4, IEEE, 2011.
- [14] A. Munari *et al.*, “Stochastic geometry interference analysis of radar network performance,” *IEEE Communications Letters*, vol. 22, no. 11, pp. 2362–2365, 2018.
- [15] P. Chu *et al.*, “Interference characterization and power optimization for automotive radar with directional antenna,” *IEEE Transactions on Vehicular Technology*, vol. 69, no. 4, pp. 3703–3716, 2020.
- [16] G. M. Brooker, “Mutual interference of millimeter-wave radar systems,” *IEEE Transactions on Electromagnetic Compatibility*, vol. 49, no. 1, pp. 170–181, 2007.
- [17] Z. Xu and Q. Shi, “Interference mitigation for automotive radar using orthogonal noise waveforms,” *IEEE Geoscience and Remote Sensing Letters*, vol. 15, no. 1, pp. 137–141, 2017.
- [18] G. Ghatak *et al.*, “Radar detection in vehicular networks: Fine-grained analysis and optimal channel access,” *IEEE Transactions on Vehicular Technology*, vol. 71, no. 6, pp. 6671–6681, 2022.
- [19] Z. Fang *et al.*, “Stochastic geometry for automotive radar interference with RCS characteristics,” *IEEE Wireless Communications Letters*, vol. 9, no. 11, pp. 1817–1820, 2020.
- [20] J. Huang *et al.*, “V2X-communication assisted interference minimization for automotive radars,” *China Communications*, vol. 16, no. 10, pp. 100–111, 2019.
- [21] M. Zhang *et al.*, “VANET-assisted interference mitigation for millimeter-wave automotive radar sensors,” *IEEE Network*, vol. 34, no. 2, pp. 238–245, 2020.
- [22] C. Aydogdu *et al.*, “RadChat: Spectrum sharing for automotive radar interference mitigation,” *IEEE Transactions on Intelligent Transportation Systems*, vol. 22, no. 1, pp. 416–429, 2019.
- [23] Y. Wang *et al.*, “Performance analysis of uncoordinated interference mitigation for automotive radar,” *IEEE Transactions on Vehicular Technology*, 2023.

- [24] Y. Wang *et al.*, "Performance analysis of coordinated interference mitigation approach for automotive radar," *IEEE Internet of Things Journal*, 2023.
- [25] M. Salehi *et al.*, "Analysis of D2D underlaid cellular networks: SIR meta distribution and mean local delay," *IEEE Transactions on Communications*, vol. 65, no. 7, pp. 2904–2916, 2017.
- [26] Y. Wang *et al.*, "On the SIR meta distribution for Poisson networks with interference cancellation," *IEEE Wireless Communications Letters*, vol. 7, no. 1, pp. 26–29, 2017.
- [27] H. ElSawy and M.-S. Alouini, "On the meta distribution of coverage probability in uplink cellular networks," *IEEE Communications Letters*, vol. 21, no. 7, pp. 1625–1628, 2017.
- [28] C. Saha *et al.*, "Meta distribution of downlink SIR in a Poisson cluster process-based HetNet model," *IEEE Wireless Communications Letters*, vol. 9, no. 12, pp. 2144–2148, 2020.
- [29] M. Shi *et al.*, "Meta distribution of the SINR for mmWave cellular networks with clusters," *IEEE Transactions on Communications*, vol. 69, no. 10, pp. 6956–6970, 2021.
- [30] Y. Wang *et al.*, "SIR meta distribution of K -tier downlink heterogeneous cellular networks with cell range expansion," *IEEE Transactions on Communications*, vol. 67, no. 4, pp. 3069–3081, 2018.
- [31] Y. Sun and Z. Ding, "A Fine Grained Stochastic Geometry-Based Analysis on LEO Satellite Communication Systems," *IEEE Networking Letters*, vol. 5, no. 4, pp. 237–240, 2023.
- [32] Y. Qin *et al.*, "On the downlink SINR meta distribution of UAV-assisted wireless networks," *IEEE Transactions on Communications*, 2023.
- [33] Y. Qin *et al.*, "On the uplink SINR meta distribution of UAV-assisted wireless networks," *IEEE Wireless Communications Letters*, vol. 12, no. 4, pp. 684–688, 2023.
- [34] J. P. Jeyaraj *et al.*, "The transdimensional Poisson process for vehicular network analysis," *IEEE Transactions on Wireless Communications*, vol. 20, no. 12, pp. 8023–8038, 2021.
- [35] K. Feng and M. Haenggi, "Separability, asymptotics, and applications of the SIR meta distribution in cellular networks," *IEEE Transactions on Wireless Communications*, vol. 19, no. 7, pp. 4806–4816, 2020.
- [36] M. Haenggi, *Stochastic geometry for wireless networks*. Cambridge University Press, 2012.
- [37] N. Abramson, "THE ALOHA SYSTEM: Another Alternative for Computer Communications," in *Proceedings of the November 17-19, 1970, Fall Joint Computer Conference, AFIPS '70 (Fall)*, p. 281–285, Association for Computing Machinery, 1970.
- [38] M. T. Shah *et al.*, "Binomial line cox processes: Statistical characterization and applications in wireless network analysis," *IEEE Transactions on Wireless Communications*, 2024.
- [39] H. S. Dhillon and V. V. Chetlur, *Poisson line Cox process: Foundations and applications to vehicular networks*. Springer, 2020.
- [40] M. Series, "Systems characteristics of automotive radars operating in the frequency band 76–81 GHz for intelligent transport. systems applications," *Recommendation ITU-R, M*, pp. 2057–1, 2014.

APPENDIX A

The proof of the above theorem follows by integrating Lemma 2, where the area of integration and limits of integration depend upon the location of ego radar and the value of R . Let us consider the following cases.

Case 1: $r_0 \in [-R_g, R_g - R]$. Here, the radar sector is completely inside the city center, i.e., within the circle of radius R_g . In Fig. 9, case 1 is marked, and the radar sector is inside only if $-R_g \leq r_0 \leq R_g - R$. Now, the average length of line segments inside this radar sector is given by integrating $\rho(r)$ over the blue area as seen in case 1 of Fig. 9 and is given as

$$2 \left(\int_0^{R \sin \Omega} \int_{mx+r_0}^{\sqrt{R^2-x^2}+r_0} \frac{n_B}{2R_g} dy dx \right) = \frac{n_B}{2R_g} \Omega R^2.$$

We will skip Case 2 and address it after Case 4.

Case 3: $r_0 \in \left(\sqrt{R_g^2 - (R \sin \Omega)^2} - R \cos \Omega, R_g \right]$. Here, the radar sector is partially inside and partially outside, as

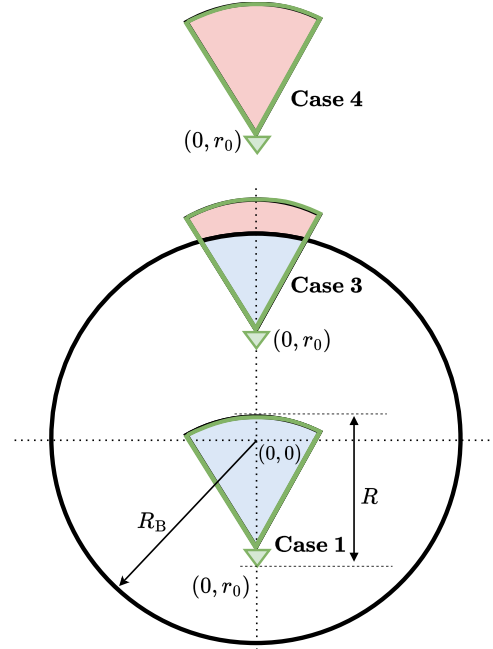


Fig. 9. Different cases of the average length of lines in BLP depending on the location of ego radar.

seen in Fig. 9. The circular arc part is outside, while the ego radar itself is present inside. This scenario occurs only if $r_0 > \sqrt{R_g^2 - (R \sin \Omega)^2} - R \cos \Omega$. If the value of r_0 lies between $R_g - R$, and $\sqrt{R_g^2 - (R \sin \Omega)^2} - R \cos \Omega$ the circular arc of the radar sector will intersect with the circular arc of the disk of radius R_g , which requires some careful analysis as we will see in Case 2. Now, in order to find l_B in this case we first integrate $\frac{n_B}{2R_g}$ over the blue area which gives

$$2 \left(\int_0^{y_C} \int_{mx+r_0}^{\sqrt{R_g^2-x^2}} \frac{n_B}{2R_g} dy dx \right) = \frac{n_B}{2R_g} \left(R_g^2 \arcsin \left(\frac{y_C}{R_g} \right) + y_C \sqrt{R_g^2 - y_C^2} - m y_C^2 - 2r_0 y_C \right).$$

Where $y_C = \frac{-mr_0 + \sqrt{R_g^2(1+m^2) - r_0^2}}{1+m^2}$ which is the intersection point between $y_C = mx + r_0$, and $x^2 + y_C^2 = R_g^2$ i.e. one of the lines of radar sector and disk of radius R_g . Following this integration, we also need to find the area of

$\frac{n_B}{\pi R_g} \arcsin \left(\frac{R_g}{\sqrt{x^2 + y^2}} \right)$ over the red area, which is given as,

$$2 \left(\int_0^{y_C} \int_{\sqrt{R_g^2-x^2}}^{\sqrt{R^2-x^2}+r_0} \frac{n_B}{\pi R_g} \arcsin \left(\frac{R_g}{\sqrt{x^2 + y^2}} \right) dy dx + \int_{y_C}^{y_B} \int_{mx+r_0}^{\sqrt{R^2-x^2}+r_0} \frac{n_B}{\pi R_g} \arcsin \left(\frac{R_g}{\sqrt{x^2 + y^2}} \right) dy dx \right).$$

Case 4: $r_0 \in \{(R_g, \infty) \cup (-\infty, -(R_g + R))\}$. Here the radar sector is completely outside the disk $\mathcal{C}((0, 0), R_g)$. Fig. 9 shows this scenario where the ego radar along with the radar sector is outside $\mathcal{C}((0, 0), R_g)$. In order to find l_B , we determine the area of $\frac{n_B}{\pi R_g} \arcsin \left(\frac{R_g}{\sqrt{x^2 + y^2}} \right)$ over the red area

only, which gives l_B as,

$$2 \int_0^{y_B} \int_{mx+r_0}^{\sqrt{R^2-x^2}+r_0} \frac{n_B}{\pi R_g} \arcsin\left(\frac{R_g}{\sqrt{x^2+y^2}}\right) dy dx.$$

Case 2 & 6: In case 3 we saw that if $\sqrt{R_g^2 - (R \sin \Omega)^2} - R \cos \Omega < r_0 \leq R_g - R$, the circular arc of radar sector will intersect with the circular arc of $\mathcal{C}((0, 0), R_g)$. This scenario gives rise to Case 2, where the ego radar is present within the disk $\mathcal{C}((0, 0), R_g)$, but the two circular arcs intersect. Likewise for case 5, if $-(R_g + R) \leq r_0 < -\sqrt{R_g^2 - (R \sin \Omega)^2} - R \cos \Omega$ the two circular arcs will again intersect, but here the ego radar is outside the disk. By first determining y_A , i.e., the point of intersection between the $x^2 + y_A^2 = R_g^2$, and $x^2 + (y_A - r_0)^2 = R^2$ i.e., the disk $\mathcal{C}((0, 0), R_g)$, and the radar sector we then integrate $\rho(r)$ to find l_B .

Case 5: This is similar to case 3, where the radar sector is partially inside the disk. Unlike case 3, here, the ego radar lies outside the disk. Thus, the circular arc of the radar sector lies inside the disk, and the remaining part lies outside. We find l_B using a similar analysis technique of case 3.